

**Kinetic electron closures for electromagnetic simulation
of drift and shear-Alfvén waves (I)**

Bruce I. Cohen, Andris M. Dimits, and William M. Nevins

University of California Lawrence Livermore National Laboratory,
Livermore, California 94550

Yang Chen and Scott Parker

Department of Physics, University of Colorado at Boulder
Boulder, CO 80309

Abstract

The electromagnetic hybrid scheme of Chen and Parker (fluid electrons and gyrokinetic ions) [Y. Chen and S. Parker, Phys. Plasmas **8**, 441 (2001)] is extended to include a kinetic electron closure valid for $\beta_e > m_e/m_i$ (β_e is the ratio of the plasma electron pressure to the magnetic field energy density). The new schemes incorporate partially linearized (δf) drift-kinetic electrons whose pressure and number density moments are used to close the fluid momentum equation for the electron fluid (Ohm's law) using the departure of the perturbed δf kinetic pressure from the isothermal perturbed pressure response. Comparisons are made between the results of the hybrid schemes with kinetic electron closure and a conventional δf algorithm for drift-kinetic electrons and gyrokinetic ions in a two-dimensional slab model. The test cases used are small-amplitude kinetic shear-Alfvén waves with electron Landau damping,

the ion-temperature-gradient instability, and the collisionless drift instability (universal mode) in an unsheared slab as a function of the plasma β_e . The hybrid schemes have the desirable properties that they do not require that the mesh size perpendicular to the applied magnetic field be smaller than the collisionless skin depth c/ω_{pe} and naturally accommodate zonal flow physics (radial modes) with non-adiabatic electron effects. The most successful of the new algorithms introduced gives very good results for $\beta_e > m_e/m_i$.

PACS numbers: 52.65.-y, 52.65.Tt, 52.35.Qz

I. INTRODUCTION

Nonadiabatic electron effects significantly modify the stability and concomitant turbulent transport of drift-waves in tokamaks. Incorporating electron kinetic and electromagnetic effects into gyrokinetic¹ particle-in-cell drift-wave turbulence simulations is computationally challenging: electrons and electromagnetics introduce additional time and space scales that alter numerical stability, increase temporal and spatial resolution requirements and, hence, increase the computational burden. Here we extend the electromagnetic hybrid scheme of Chen and Parker² (fluid electrons and gyrokinetic ions) to include a kinetic electron closure valid for $\beta_e m_i / m_e \gg 1$ where $\beta_e = 4\pi n_e T_e / B^2$, T_e is the electron temperature, and B is the magnetic field strength. We introduce a new closure scheme that makes particle simulation of electromagnetic drift-wave turbulence with drift-kinetic electrons and gyrokinetic ions tractable with realistic mass ratios and realistic β_e .

The new family of algorithms incorporates partially linearized^{3,4} δf drift-kinetic electrons whose pressure and number density moments are used to close the fluid momentum equation for the electron fluid (Ohm's law). Comparisons are made between the results of the hybrid schemes with kinetic electron closure and a conventional δf algorithm for drift-kinetic electrons and gyrokinetic ions in a two-dimensional slab model. The test cases used are small-amplitude kinetic shear-Alfven waves with electron Landau damping, the ion-temperature-gradient instability, and the collisionless drift instability (universal mode) in an unsheared slab as a function of β_e . The hybrid schemes have the desirable properties that they do *not* require that the mesh size perpendicular to the applied magnetic field be smaller than the collisionless skin depth c/ω_{pe} and naturally accommodate zonal flow physics (radial modes⁵) with non-adiabatic electron

effects. Two of the three new hybrid schemes use a variation of the split-weight scheme introduced by Manuilsky and Lee.⁶ In this case the electron distribution function f_e is given by

$$f_e = f_M(\vec{x}, \vec{v}) + (\delta n_e^{(0)} / n_0) f_M(\vec{x}, \vec{v}) + h_e(\vec{x}, \vec{v}), \quad (1)$$

where f_M is a Maxwellian velocity distribution function including possible equilibrium temperature and density gradients, n_0 is the equilibrium electron density, $\delta n_e^{(0)}$ is the lowest-order fluid approximation to the total electron density perturbation (more explicitly defined in Sec. II), and h_e is the non-adiabatic part of the electron density perturbation determined using a variant of the δf method. Use of the split-weight algorithm is found to be efficacious in that statistical noise arising from the particle representation is relegated to the relatively small h_e term in Eq.(1). The most successful of the new algorithms introduced here for the kinetic electron extension of the hybrid scheme of Chen and Parker gives very good results for $\beta_e m_i / m_e \ll 1$ and poor results in the opposite limit.

The work presented here departs from earlier work^{7,8,9,10} in several respects. The research of Reynders⁷ and Cummings⁸ did not use split-weight methods nor hybrid techniques, and their algorithms could not efficiently address plasma conditions for which $\beta_e m_i / m_e \gg 1$. The research of Cohen and Dimits⁹ used implicit δf methods, did not use split-weight methods, and did not address $\beta_e m_i / m_e \gg 1$ plasma conditions. Chen and Parker have modeled kinetic electrons in three-dimensional toroidal simulations using parallel canonical momentum and a variant of the split-weight scheme; however, their simulations were still limited to $\beta_e m_i / m_e \ll 1$. The approach taken here in the most successful new algorithm introduced resembles in some respects the recent work of Lin and Chen¹¹ who have introduced a new split-weight algorithm and applied it to the propagation of small-amplitude shear-Alfvén waves in a uniform plasma. The physics content underlying our new algorithms presented here is as follows. First we

recognize that the nonadiabatic kinetic components of the low-order velocity moments of the perturbed electron velocity distribution are small perturbations to the dominantly fluid response for the low-frequency phenomena of interest (shear-Alfvén and low-frequency drift-type modes). This allows us to extend the hybrid model introduced by Chen and Parker rigorously with a perturbative correction that captures the nonadiabatic kinetic increment to the electron response for use in the moment and field equations. This is described in detail in Sec. IIB. In addition to test cases simulating shear-Alfvén waves in a uniform plasma, the work here addresses the collisionless drift and ion-temperature gradient instabilities in both linear (single mode) and two-dimensional nonlinear (many mode) simulations in non-uniform plasmas, and accommodates the nonlinear generation of zonal flows (radial modes⁵) not addressed in the work of Lin and Chen.¹¹

The remainder of the paper is organized as follows. In Section II we present two algorithms (conventional δf with drift-kinetic electrons and gyrokinetic ions following Cummings' work⁷ and Hybrid II, an extension of the Chen and Parker hybrid model² with massless fluid electrons and gyrokinetic ions in which kinetic electron closures are added) that are used for electromagnetic drift-wave turbulence simulations. Section III contains comparisons of the performance of the algorithms to the linear analytical theory for the propagation and damping of small-amplitude shear-Alfvén waves, the frequencies and growth rates for small-amplitude collisionless drift and ion-temperature gradient (ITG) instabilities, and simulation results for many mode simulation of the linear growth and nonlinear saturation in two spatial dimensions of an ITG instability for several different values of β_e . In Section IV we present simulation results that address how large a time step can be used in our simulations. In Section V, we discuss the general accuracy and stability characteristics of the algorithms, and summarize

the results. Two additional hybrid algorithms (Hybrid I and Hybrid III) whose performance is not as good as that of Hybrid II are described in the Appendix.

II. ELECTROMAGNETIC ALGORITHMS FOR KINETIC SIMULATION OF DRIFT AND SHEAR-ALFVÉN WAVES

In this section we describe the basic ingredients of a conventional δf algorithm with drift-kinetic electrons and gyrokinetic ions and a family of algorithms that add kinetic electron closures to the Chen and Parker hybrid scheme.²

A. Conventional δf Algorithm With Canonical Momentum

To establish a benchmark against which we will compare the performance of the new algorithms that are introduced here, we have used Cummings⁷ basic algorithm for simulating drift waves and shear-Alfvén waves. Ions are described as δf gyrokinetic particles, and their trajectories are advanced with a predictor-corrector scheme using a time step Δt_i that is the same as that used in the solution of the field equations. Electrons are described as δf drift-kinetic particles, and their trajectories are advanced with a predictor-corrector scheme using a time step Δt_e that is an integer sub-multiple of the ion time step. The use of electron subcycling is a departure from Cummings' algorithm. Electron and ion currents and charge densities are accumulated from the particles at each Δt_i and used in Ampere's law to determine the magnetic vector potential and in a quasi-neutrality equation to determine the electrostatic potential.

The ions and electrons satisfy the gyrokinetic reduced Vlasov-Maxwell equations^{8,10,12} with the following orderings:

$$\frac{\delta f_{e,i}}{F_M^{e,i}} \sim \frac{e\phi}{T} \sim \frac{|\delta \mathbf{B}|}{B} \sim \frac{\omega}{\Omega_i} \sim \frac{\rho_i}{L} \sim \epsilon \ll 1 \quad \text{and} \quad L \sim L_{\parallel}, \quad (2)$$

where $\rho_i = v_i / \Omega_i$ is the ion Larmor radius defined as the ratio of the ion thermal velocity to the ion cyclotron frequency, $\Omega_i = qB / m_i c$, $v_i = (T_i / m_i)^{1/2}$, q , m_i , and T_i , respectively, are the ion

charge, mass, and temperature; c is the speed of light, B is the equilibrium magnetic-field strength, $\delta\vec{\mathbf{B}}$ is the perturbed magnetic field, ϕ is the electrostatic potential, ω is the frequency of the field perturbation, L is a characteristic perpendicular equilibrium scale length of the system; and L_{\parallel} is the characteristic parallel wavelength of the perturbation. We use a multi-scale treatment throughout this work.^{1,4,5} The electric and magnetic fields are given by

$$\vec{\mathbf{E}} = -\vec{\nabla}\phi - c^{-1}\partial\vec{\mathbf{A}}_{\parallel}/\partial t, \vec{\mathbf{B}} = \vec{\mathbf{B}}_0 + \nabla\phi \times \hat{\mathbf{z}}/B_0 = B_0\hat{\mathbf{z}} + B_y^{(0)}\hat{\mathbf{y}} + \nabla\phi \times \hat{\mathbf{z}}. \quad (3)$$

The electron and ion kinetic distribution functions are represented by

$$f_{e,i} = F_M^{e,i} + \delta f_{e,i}(\vec{\mathbf{x}}, \vec{\mathbf{v}}, t), \quad \delta f_{e,i} = \sum_i w_i^{e,i} \delta(\vec{\mathbf{x}} - \vec{\mathbf{x}}_i) \delta(\vec{\mathbf{v}} - \vec{\mathbf{v}}_i). \quad (4)$$

The equilibrium distribution functions $F_M^{e,i}$ are Maxwellians in the parallel velocity and the magnetic moment, and the parallel velocity can be replaced by the initial canonical momentum parallel to the magnetic field as the independent variable. The marker particles in our simulations are initialized in velocity space using a Maxwellian distribution. The partially linearized gyrokinetic ion and drift-kinetic electron Vlasov equations for a plasma with weak magnetic shear in slab geometry are^{13,14}

$$\frac{\partial \delta f_i}{\partial t} + v_{\parallel} \hat{\mathbf{b}} \cdot \frac{\partial \delta f_i}{\partial \mathbf{R}} - \frac{c}{B} \frac{\partial}{\partial \mathbf{R}} \cdot \left(\frac{\partial \bar{\phi}}{\partial \mathbf{R}} \times \hat{\mathbf{b}} \right) \delta f_i = \frac{v_{\parallel}}{v_i^2} \dot{p}_{\parallel} F_M^i - \kappa_i \left(\frac{c}{B} \frac{\partial \bar{\phi}}{\partial y} - \frac{v_{\parallel}}{B} \frac{\partial \bar{A}_z}{\partial y} \right) F_M^i \quad (5)$$

$$\frac{\partial \delta f_e}{\partial t} + v_{\parallel} \hat{\mathbf{b}} \cdot \frac{\partial \delta f_e}{\partial \mathbf{R}} - \frac{c}{B} \frac{\partial}{\partial \mathbf{R}} \cdot \left(\frac{\partial \phi}{\partial \mathbf{R}} \times \hat{\mathbf{b}} \right) \delta f_e = \frac{v_{\parallel}}{v_e^2} \dot{p}_{\parallel} F_M^e - \kappa_e \left(\frac{c}{B} \frac{\partial \phi}{\partial y} - \frac{v_{\parallel}}{B} \frac{\partial A_z}{\partial y} \right) F_M^e \quad (6)$$

in terms of the parallel canonical momentum per unit mass $p_{\parallel} = v_{\parallel} + q_s A_z / m_s c$, where

$$\hat{\mathbf{b}} = \hat{\mathbf{z}} + \hat{\mathbf{y}} B_y^{(0)} / B_0 + \nabla\phi \times \hat{\mathbf{z}} / B_0, \quad \hat{\mathbf{b}}^{(0)} = \hat{\mathbf{z}} + \hat{\mathbf{y}} B_y^{(0)} / B_0,$$

$\kappa_s = -\ln F_M^s = \kappa_{ns} \left[1 + \eta_s \left(v^2 / 2v_s^2 - 3/2 \right) \right]$, κ_{ns} is the magnitude of the density gradient for

species s , $\eta_s = d \ln T_s / d \ln n_s$, $\dot{p}_{||} = -(q_s / m_s) \hat{\mathbf{b}}^{(0)} \cdot (\nabla \phi + (q_s / m_s) v_{||} \nabla_z / c)$,⁸

$$\bar{\phi} = \frac{1}{2\pi} \oint d\mu \hat{\rho} \phi(\bar{\mathbf{R}} + \bar{\rho}) \quad (7)$$

and analogously for \bar{E} , etc., $\bar{\mathbf{R}} = \bar{\mathbf{x}} - \bar{\rho}$, $\bar{\rho} = \bar{\mathbf{v}} \times \hat{\mathbf{b}} / \Omega_i$, $\hat{\rho}$ is a unit vector in the direction of $\bar{\rho}$ (the integral in Eq.(7) is an integral around the Larmor orbit with respect to the gyrophase angle),

$\bar{\mathbf{x}}$ is the particle position vector, $\bar{\mathbf{v}}$ is the perpendicular velocity, $\delta f_{e,i}(\bar{\mathbf{R}}, \mu, v_{||}, t)$ is the

gyroaveraged perturbed distribution function, and $\mu = v^2 / 2$. The electrons have a vanishingly small Larmor radius. The electrostatic potential ϕ is given by the gyrokinetic Poisson equation, which for a single-ion species (species subscript i and singly charged), is given by

$$\nabla^2 \phi - \frac{\tau(\phi - \tilde{\phi})}{\lambda_D^2} = 4\pi e (\delta \bar{n}_i - \delta n_e), \quad (8a)$$

where

$$\tilde{\phi}(\bar{\mathbf{x}}) = \frac{1}{2\pi} \oint d\mu \hat{\rho} \phi(\bar{\mathbf{x}} - \bar{\rho}), \quad (8b)$$

$\tau = T_e / T_i$, $\lambda_D^2 = T_e / 4\pi n_0 e^2$ is the square of the electron Debye length, n_{0e} is the unperturbed electron density, $\delta \bar{n}_i$ is the gyroaveraged perturbed ion density, δn_e is the perturbed electron density, and for simplicity we have assumed that the ions are singly charged. The angle averages indicated in $\delta \bar{n}_i$ and $\bar{\phi}$ are replaced by averages over four points on the ion Larmor orbit. The field interpolations from the grid to the particles and the deposition of distribution function

moments from the particles onto the grid involve spatial weighting functions.¹ Ampere's law determines the parallel component of the vector potential:

$$-\nabla^2 A_z = \frac{4\pi}{c} (j_{e\parallel} + j_{i\parallel}), \quad (9)$$

and the parallel currents are computed to lowest significant order from the distribution functions expressed in terms of the canonical parallel momentum per unit mass,

$$j_{s\parallel} = \int d\mathbf{u} dp_{\parallel} (p_{\parallel} - q_s A_z / m_s c) (F_M^s + \delta f_s). \quad (10)$$

Here the equilibrium density gradients are in the x direction, and the unperturbed magnetic field has its principal component in the z direction with a small component in the y direction. With no magnetic shear $B_y^{(0)}$ is a constant, and with shear $B_y^{(0)} = B_0(x - x_0) / L_s$, where L_s is the magnetic shear length. In the unsheared slab, all quantities are subject to periodic boundary conditions. In the sheared slab, the electric and vector potentials satisfy Dirichlet boundary conditions in x and are periodic in y .⁷⁻⁹ The gyrokinetic ion particle equations of motion are given by

$$d\bar{\mathbf{x}} / dt = \bar{\mathbf{v}} \quad \bar{\mathbf{v}} = \bar{\mathbf{v}}_{\parallel} + \langle \bar{\mathbf{v}}_{\perp} \mathbf{E} \times \mathbf{B} \rangle \quad (11a)$$

$$\frac{dw_j^i}{dt} = \left\langle \frac{-ev_{\parallel}}{T_e} \bar{\phi} + \frac{v_{\parallel}^2}{v_e^2} \left(\frac{eA_z}{m_e c} - \kappa_i \left(\frac{c}{B} \frac{\partial \phi}{\partial y} - \frac{v_{\parallel} \tilde{B}_x}{B} \right) \right) \right\rangle, \quad (11b)$$

where the angle brackets on the right sides of Eq.(11a) and (11b) indicate a four-point average around the ion Larmor orbit, $\bar{\mathbf{b}}^{(0)}$, and w_j^i are the ion particle weights. The corresponding drift-kinetic electron particle equations of motion are given by

$$d\vec{x}/dt = \vec{v} \quad \vec{v} = \vec{v}_{\parallel} + \vec{v}_{\perp} \times \mathbf{B} \quad (12a)$$

$$\frac{dw_i^e}{dt} = \frac{ev_{\parallel}}{T_e} \phi - \frac{v_{\parallel}^2}{v_e^2} \frac{(0)}{\parallel} \phi - \frac{(0)}{\parallel} \frac{eA_z}{m_e c} - \kappa_e \left(\frac{c}{B} \frac{\partial \phi}{\partial y} - \frac{v_{\parallel} \tilde{B}_x}{B} \right). \quad (12b)$$

Because of the partial linearization^{3,4} no parallel wave trapping of ions or electrons is allowed, and v_{\parallel} is a constant for both species. With A_z initialized to a small value, the *initial* parallel canonical momenta per unit mass for both electrons and ions are equal to the parallel velocities and are trivial constants of the motion (the parallel canonical momenta are *not* constant in time; only the initial conditions are constants of the motion). The electron equations of motion employ a time step Δt_e that is constrained to be an integer sub-multiple of Δt_i where $\Delta t_i = N_{sub} \Delta t_e$ and N_{sub} is the subcycling parameter. The predictor-corrector time integration of Eqs.(11) and (12), and the solution of the field equations (3), (8), and (9) require that all quantities be defined at integer time steps $N\Delta t_i$ so that electron charge and parallel current densities need only be accumulated at the end of the subcycling interval and not at each electron time step (no electron orbit-averaging¹⁵ is undertaken here).

B. Hybrid II Algorithm

Here we introduce a kinetic electron extension of the Chen and Parker hybrid algorithm. Two other extensions of the Chen and Parker hybrid algorithm are described briefly in the Appendix. In this algorithm we employ the *split-weight* electron distribution function in Eq.(1).⁶ Consider the modified electron momentum equation (Ohm's law) derived from the parallel velocity moment of the electron drift-kinetic equation Eq.(6):

$$en_0 \vec{E} \cdot \hat{\mathbf{b}} = - \parallel P_{\parallel e} - n_0 m_e (\partial / \partial t + \vec{v}_{\perp} \times \mathbf{B} \cdot \nabla) u_{\parallel e}, \quad (13a)$$

where $\parallel \hat{\mathbf{b}}$, with the following prescription for the pressure term used in Ref. 2 and rigorously justified in Ref. 16 for the orderings in Eq.(2):

$$\parallel P_{\parallel e} = \parallel P_{\parallel e}^{(0)} + T_{\parallel e}^{(0)} \parallel \delta n_e^{(0)} + n_{0e} \parallel \delta T_{\parallel e} = \parallel P_{\parallel e}^{(0)} + T_{\parallel e}^{(0)} \parallel (\delta n_e - \Delta n_e^K) + n_{0e} \parallel \delta T_{\parallel e}, \quad (13b)$$

using Eq.(1) to make the substitution $\delta n_e^{(0)} = \delta n_e - \Delta n_e^K$, where $\delta n_e^{(0)}$ used in Eqs.(1) and (13b) is the lowest-order fluid component of the total perturbed electron density,

$$\parallel (T_{\parallel e}^{(eq)} + \delta T_{\parallel e}) = 0, \quad T_{\parallel e}^{(eq)} \text{ is the equilibrium temperature (including gradients),}$$

$$P_{\parallel e}^{(0)} = n_e^{(0)} T_{\parallel e}^{(eq)}, \quad n_e^{(0)} \text{ is the equilibrium density (including gradients), } T_{\parallel e}^{(0)} \text{ is a constant and}$$

$\Delta n_e^K = d^3 \mathbf{v} h_e$ is the split-weight kinetic electron *increment* to the charge density. We note that

$\delta n_e = \delta n_e^{(0)} + \Delta n_e^K$ is the total perturbed electron density including kinetic corrections as

determined by Eq.(1). Equation (13b) in concert with Eq.(13a) represents the adiabatic electron fluid parallel pressure consistent with Ref. 16. Non-adiabatic kinetic corrections in the parallel pressure in Eq.(13b) derived from the second parallel velocity moment of Eq.(1) are higher order in $(\omega / k_{\parallel} v_e)^2$ than are the terms in Eq.(13b) coming from the adiabatic response. The

representation of the perturbed electron density as an expansion around the fluid density is

similar to Ref. 11. In our formulation the expansion parameter is $|\Delta n_e^K / \delta n_e^{(0)}| < 1$. With the

result of Eq.(13a) for $\parallel P_{\parallel e}$ substituted into Eq(13a), Eq.(13a) is the rigorous analogue of

Eq.(15) in Ref. 11. However, our complete equation set incorporates radial modes

($k_{\parallel} = 0, k \neq 0$) naturally, while the formulation in Ref. 11 requires extension.

Ohm's law, Eq.(13a) using (13b) for the pressure gradient, is used to obtain E_{\parallel} . This electric field together with $\partial A_z / \partial t = c(\bar{\mathbf{E}} + \phi) \cdot \hat{\mathbf{b}}^{(0)}$ is used to advance A_z in time. With the updated A_z , Ampere's law determines the parallel electron current:

$$n_{0e} u_{\parallel e} = \frac{c}{4\pi e} \nabla^2 A_z + \bar{\Gamma}_{\parallel i}, \quad (14)$$

where $\bar{\Gamma}_{\parallel i}$ is the gyrokinetic parallel ion current per unit charge. The electron continuity equation deduced from the velocity-space integral of Eq.(6) provides the prescription for advancing the total electron density ahead in time:

$$\frac{\partial \delta n_e}{\partial t} + n_{0e} (\bar{\mathbf{B}}^{(0)} + \delta \bar{\mathbf{B}}) \cdot \frac{\mathbf{u}_{\parallel e}}{B} + \bar{\mathbf{v}} \cdot \mathbf{E} \times \mathbf{B} \cdot \nabla n_e = 0 \quad (15)$$

where $n_e = n_e^{(0)} + \delta n_e$. Curvature and gradient-B drifts and toroidal effects can be readily included in these equations.^{2,16} The electrostatic potential is obtained from the quasi-neutral form of Eq.(8) suppressing the first term on the left side of Eq.(8a) and using the updated total electron and ion charge densities. The evolution of the gyrokinetic ion and the drift-kinetic electron positions and weights deduced from Eqs.(12a) and (12b) using a parallel velocity representation (p_{\parallel} , v_{\parallel} and $\dot{p}_{\parallel} = q_s \bar{\mathbf{E}} \cdot \hat{\mathbf{b}}$ in the kinetic equations) is computed using a predictor-corrector time integration, and there is no electron subcycling here (after cancellations obtained by using Eqs.(13) and (15)),

$$\frac{dw_j^i}{dt} = \frac{ev_{\parallel}}{T_i} \bar{E} \cdot \hat{\mathbf{b}} - \kappa_i \left[\frac{e}{B} \frac{\partial \phi}{\partial y} - \frac{v \delta B_x}{B} \right] \quad (16a)$$

$$\frac{dw_j^e}{dt} = \bar{\kappa}_e \cdot \bar{\mathbf{v}} \cdot \mathbf{E} \times \mathbf{B} + (\kappa_e - \kappa_{ne}) v_{\parallel} \frac{\delta B_x}{B_0} - \frac{\partial \delta n_e^{(0)} / n_0}{\partial t} - \bar{\mathbf{v}} \cdot \mathbf{E} \times \mathbf{B} \cdot \nabla n_e^{(0)} / n_0 + (v_{\parallel} / v_e^2) \left(\frac{\partial}{\partial t} + \bar{\mathbf{v}} \cdot \mathbf{E} \times \mathbf{B} \cdot \nabla \right) u_{\parallel e}$$

$$(\bar{\mathbf{v}} \cdot \mathbf{E} \times \mathbf{B} \cdot \hat{\mathbf{x}} + v_{\parallel} \frac{\delta B_x}{B_0}) \kappa_{Te} \left(\frac{v^2}{v_e^2} - \frac{3}{2} \right) + u_{\parallel e} + (v_{\parallel} / v_e^2) \left(\frac{\partial}{\partial t} + \bar{\mathbf{v}} \cdot \mathbf{E} \times \mathbf{B} \cdot \nabla \right) u_{\parallel e}, \quad (16b)$$

where we have used the lowest-order approximation $\delta n_e \approx \delta n_e^{(0)}$ in the continuity equation employed in obtaining the final expression on the right side of (16b), which makes explicit use of the small parameter $|\Delta n_e^K / \delta n_e^{(0)}|$ in our perturbation expansion and is consistent with the formal expansion procedure in Ref. 11. The angle brackets in Eq.(16a) indicate the four-point gyro-average of the field quantities on the right side of the ion weight equation. The parallel electric field in Eq.(16a) is determined by Eq.(8) for the electrostatic field and Eq.(13a) for the electromagnetic contribution. The last terms on the right side of Eq.(16b) arise from the electron inertia terms in Eq.(13a), $-n_0 e m_e (\partial / \partial t + \vec{v} \times \mathbf{B} \cdot \nabla) u_{\parallel e}$. To accommodate the electron inertia terms, we used an explicit uncentered finite difference in time in the predictor step of the predictor-corrector time integration of Eqs.(13-16). With the exception of the electron inertia terms, the predictor-corrector integration of the entire system is second-order accurate in time. Retention or omission of the electron inertia terms had no significant influence on any of the simulation results obtained. Our attempts so far to include electron subcycling in the hybrid schemes have led to numerical instability.

This algorithm has several advantages. By introducing the split-weight decomposition, particle noise only enters through the non-adiabatic component of f_e , which is presumably small for phenomena with parallel phase velocities much smaller than the electron thermal velocity. Thus, a significant noise reduction is expected.⁶ Although the fluid quantities are subject to the constraint $\nabla_{\parallel} (T_{\parallel e}^{(eq)} + \delta T_{\parallel e}) = 0$, the Hybrid II algorithm accommodates finite η_e in the simulations. Furthermore, this algorithm requires only the lowest moment of the non-adiabatic electrons, viz., Δn_e^K ; no parallel electron current or pressure moment must be computed in this model at this stage.

III. TEST SIMULATIONS

In this section we report the results of test simulations comparing the results of the conventional δf algorithm and the Hybrid II algorithm. The test cases considered are kinetic shear-Alfvén waves (including electron Landau damping), the collisionless-drift instability, and the ion-temperature-gradient instability. The algorithms have been implemented in a two-dimensional slab geometry with either Dirichlet or periodic boundary conditions for simulations with or without magnetic shear. The test cases reported here have no magnetic shear (see Refs. 7, 8 and 9 for examples of sheared slab simulations).

A. Shear-Alfvén Waves

With a finite- β ordering, $m_e/m_i \ll 1$, the electrons are dominantly adiabatic but have important nonadiabatic kinetic corrections in their response to electric fields. Shear-Alfvén waves and magnetized sound waves are the two fluid normal modes in a slab geometry with a uniform plasma, $k_{\parallel} \ll k$ and $\omega \ll \Omega_i \ll \Omega_e$, where k_{\parallel} is the wavenumber component parallel to the equilibrium field and $\Omega_{e,i}$ are the electron and ion cyclotron frequencies. The linear dispersion relations for shear-Alfvén waves and sound waves in this system are derived from⁷⁻⁹

$$\chi_{\perp i} + \frac{k_{\parallel}^2}{k^2} (\chi_{\parallel e} + \chi_{\parallel i}) \left(1 - \frac{\omega^2}{k_{\parallel}^2 c^2} \chi_{\perp i}\right) = 0, \quad (17)$$

where the perpendicular and parallel ion susceptibilities are given by

$$\chi_{\perp i} = (\omega_{pi}^2 / \Omega_i^2) (1 - I_0 e^{-b}) / b - (\omega_{pi}^2 / \Omega_i^2) (1 - k^2 \rho_i^2) \quad \text{and} \quad \chi_{\parallel s} = -(\omega_{ps}^2 / 2k_{\parallel}^2 v_s^2) Z(\omega / \sqrt{2} k_{\parallel} v_s),$$

and Z' is the derivative of the plasma dispersion function. At leading order the electron

susceptibility is given by $\chi_{\parallel e} = 1 / k_{\parallel}^2 \lambda_e^2 + \dots$. Solution of this dispersion relation yields shear-

Alfvén and magnetized sound wave branches that are well separated if $c_s^2/v_A^2 = \beta \ll 1$, where $c_s = (T_e/m_i)^{1/2}$ is the sound velocity,

$$\omega^2 = k_{\parallel}^2 v_A^2 (1 + k^2 \rho_s^2 + k^2 \rho_i^2) \quad (18a)$$

$$\omega^2 = k_{\parallel}^2 c_s^2 (1 + k^2 \rho_s^2) \quad (18b)$$

in the fluid limit for Alfvén waves and sound waves, respectively. All of the algorithms considered here are subject to a Courant condition for stability determined by these normal modes: $(B_y^{(0)}/B_0) \max(c_s, v_A) \Delta t \leq \Delta y$.

We first consider simulation results obtained using the conventional δf algorithm. In these simulations we introduced a modification to Ampere's law Eq.(9) to account for the linear interpolation that occurs in the simulation code between the particles and the grid so that Ampere's law becomes

$$-k_{\parallel}^2 + S^2(k_x, k_y) \frac{\omega_{ps}^2}{c^2} \frac{eA_{\parallel}}{m_e c} = - \frac{\omega_{ps}^2}{c^2} \langle p_{\parallel s} \rangle, \quad (19)$$

where $\langle p_{\parallel s} \rangle = d^3 v \delta f_s p_{\parallel}$ and $S^2 = [\sin(k_x \Delta x / 2) / (k_x \Delta x / 2)]^2 [\sin(k_y \Delta y / 2) / (k_y \Delta y / 2)]^2$ for linear interpolation between the grid and the particles¹⁷ to match the corresponding grid dependence of the right side of Eq.(19) in the limit of small-amplitude waves.

In Fig. 1 we present results from conventional δf simulations of kinetic shear-Alfvén waves. Plotted are scans of $Re \omega/\Omega_i$ and $Im \omega/\Omega_i$ vs. $\Delta y \omega_{pe}/c$ and β_e for $k_y \rho_s = \pi/8$, $T_e = T_i$, $B_y^{(0)}/B_0 = 0.01$, $\rho_s = 4\Delta y$, a 64×64 grid, either 4, 9, or 16 electrons and ions per two-dimensional cell, only the (0,1) mode (in this figure points marked “o” designate no grid correction in

Ampere's law; "x" is with the grid correction; and the dashed line is theory). In these examples the Alfvén speed is less than or equal to the electron thermal velocity and large compared to the ion thermal velocity: $v_A/v_e = 1/(\beta_e m_i/m_e)^{1/2}$, $v_A/v_i = 1/\beta_e^{1/2}$. In consequence, electron Landau damping is the dominant dissipation mechanism. The agreement with theory is quite good until $\Delta y \omega_{pe}/c > 1$ and gets progressively worse as the skin depth becomes smaller than the grid spacing (or, equivalently, β_e increases). The error in our measurement of frequencies and growth rates in all of the simulation data is a few percent or less. The inclusion of the grid-correction factor S^2 provides some benefit in improving the agreement of the simulations with theory. The failure of the conventional δf algorithm to yield correct results when the skin depth is not resolved by the grid has been documented previously by Cummings.⁸ Our interpretation of the computational difficulty is that in order for the solution of Eq.(19) to be accurate, errors in the resolution of the ω_{pe}^2/c^2 term and the corresponding cancellations originating from within the right side of Eq.(19) must be small compared to the $-\omega^2$ term on the left side. Inclusion of the S^2 coefficient helps the cancellations to occur with greater precision, but this omits the particle statistical aspect of the cancellations in the total electron parallel current response. Thus, a computational stiffness problem arises and persists when the skin depth is small, which occurs when the first term on the left side of Eq.(19), of order $O(k^2 \rho_s^2)$ where ρ_s is the ion Larmor radius using the electron temperature, is small compared to the second term, which is of order $O(\omega_{pe}^2 \rho_s^2 / c^2 = \beta_e m_i / m_e)$.

In Figure 2 we present a comparison of the results of the Hybrid II simulations of kinetic shear-Alfvén waves and linear theory. Plotted are scans of $Re \omega/\Omega_i$ and $Im \omega/\Omega_i$ vs. β_e for $k_y \rho_s = 1/8$, $\rho_s = 2\Delta y$, a 32×32 grid, and other parameters that are the same as in Fig. 1. Hybrid II results

are denoted with “o” and Hybrid III (see Appendix) results with “x”. The dashed curve is linear theory. The agreement with theory is excellent when $\beta_e m_i / m_e > 1$. The hybrid algorithms become unstable for $\beta_e m_i / m_e < 1$; these algorithms cannot recover the electrostatic limit because of the “backwards” solution of Eq.(14). In the electrostatic limit, $\beta_e m_i / m_e < 1$, Eq.(14) should not have been retained in the system of equations. Thus, it is not surprising that there are significant difficulties in the hybrid schemes for $\beta_e m_i / m_e < 1$. There is no requirement that the skin depth be resolved. These results resemble those obtained in the independent work of Lin and Chen.¹¹

B. Collisionless Drift-Wave Instability

In Fig. 3 we present examples of conventional δf simulation of collisionless drift-wave instability. Scans of $Re\omega/\Omega_i$ and growth rate $Im\omega/\Omega_i$ vs. β_e are plotted for $k_y \rho_s = 1/4$, $\rho_s/L_n = 0.2$, $T_e = T_i$, $B_y^{(0)}/B_0 = 0.01$, $\rho_s = 8\Delta y$, 64×64 grid, $\Delta y = 0.5c/\omega_{pe}$, no magnetic shear, and only the (0,1) mode retained. The dashed curves indicate linear theory.⁸ Good results are obtained when the skin depth is resolved. Data from a second series of collisionless drift-wave simulations with the conventional δf algorithm are plotted in Fig. 4. In Fig. 4 the ratio of the grid cell size to the skin depth increases with β_e and exceeds unity for some of the simulations, which results in a degradation of the accuracy of the results compared to linear theory. In Fig. 4 we plot $Re\omega/\Omega_i$ and $Im\omega/\Omega_i$ vs. $\omega_{pe} \Delta y/c$ and β_e for $k_y \rho_s = 1/4$, $\rho_s/L_n = 0.2$, $T_e = T_i$, $B_y^{(0)}/B_0 = 0.01$, $\rho_s = 2\Delta y$, 16×16 grid, no magnetic shear, and only the (0,1) mode retained. Data points denoted with “o” include the grid correction introduced in Eq.(19), and points denoted with “x” omit this correction. A systematic error emerges in the results obtained when $\Delta y > c/\omega_{pe}$ in the conventional δf algorithm.

The Hybrid II algorithm yielded very good results for simulations of the collisionless drift-wave instability. In Fig. 5 we plot $Re\omega/\Omega_i$ and growth rates $Im\omega/\Omega_i$ from Hybrid II and

conventional δf simulations vs. β_e and $\omega_{pe} \Delta y/c$ for the same parameters as those defined in Fig.

4. The standard δf simulation with the grid correction in Ampere's law gives good results only for $\beta m_i/m_e \ll O(1)$ and $\Delta y < c/\omega_{pe}$, while the Hybrid II algorithm gives good results for $\beta m_i/m_e > 1$ and any skin depth.

C. Ion-Temperature-Gradient Instability

Our conventional δf slab simulations of unsheared ion-temperature-gradient instability (ITG) with S^2 particle-grid interpolation factor correction to the inverse skin-depth term in Ampere's law demonstrate finite- β stabilization and good agreement with linear theory when the cell size is smaller than the skin depth, i.e., $\Delta x < c/\omega_{pe}$. Frequency and growth rates for the (0,1) mode ($k_y \rho_s = \pi/8$) are plotted in Fig. 6 as a function of $\omega_{pe} \Delta x/c$ and β_e , where

$\beta_e = (\omega_{pe} \Delta x/c)^2 (\rho_s/\Delta x)^2 (m_e/m_i) (\omega_{pe}/\Omega_e)^2$, there is no magnetic shear, $B_y^{(0)}/B_0 = 0.01$, $T_e = T_i$, $\eta_e = \eta_i = 4$, $\rho_s/L_n = 0.1$, $\rho_s = 4 \times$, $\Omega_e/\omega_{pe} = 1$, $m_i/m_e = 1836$, and 64×64 grid. Theory⁸ is shown with a dashed curve. Data from simulations with $N_{sub} = \Delta t/\Delta t_e = 4$ are denoted by “o” and with $N_{sub} = 5$ by “x.”

The Hybrid II algorithm is able to accommodate finite η_e . In Fig. 7 and Table I we present results from Hybrid II simulations of ITG for a single linear mode with $k_y \rho_s = \pi/8$, $\rho_s = 2\Delta x$, 32×32 grid, $\eta_e = 4$ and other physical parameters the same as for the Hybrid I simulation data in Fig. 6. The Hybrid II simulations of unsheared ITG agree relatively well for $\beta m_i/m_e > 1$, and there is no constraint on the skin depth, c/ω_{pe} , relative to the cell size Δx . Linear theory is indicated by the dashed curve in Fig. 7. The results in Table I quantify the influence of finite η_e on ITG for these specific parameters.

D. Nonlinear Simulations of Ion-Temperature-Gradient Instability

Comparisons of simulation results with linear theory are only one kind of test for determining the reliability of a new simulation algorithm. Because a primary motivation for the introduction of these algorithms is the study of the nonlinear saturation of drift-type instabilities and the concomitant transport of energy and particles across the density and pressure gradients in the plasma, it is necessary that the simulation algorithms produce sensible nonlinear results. Earlier simulation work^{1,4,5,7-9} has concluded that the slab, multi-scale physics model with kinetic electrons and ions presented here should lead to saturated states with the radial modes^{5,8,9} playing an important role.

In Figs. 8 and 9 we present results of nonlinear simulations of ITG instability performed with the conventional δf and Hybrid II algorithms showing linear growth followed by nonlinear saturation mediated by the nonlinear generation of radial modes ($k_y=0, k_x \neq 0$). Nonlinear, many-mode, two-dimensional slab simulation results with no shear, $B_y^{(0)}/B_0=0.01$, $T_e=T_i$, $\eta_i=\eta_e=4$, $\rho_s/L_n=0.1$, $\Omega_e/\omega_{pe}=1$, $m_i/m_e=1836$, $\rho_s=\Delta x$, 16×16 grid, and $\Delta t c_s/L_T=0.4$ are presented. Super-gaussian k-space smoothing, $\exp(-k^4 a^4)$, was used in the conventional δf code, and a Heaviside-function was used in the Hybrid II algorithm (modes were suppressed completely for $k^2 a^2 > 1$, with $a=1$ in both algorithms). When super-gaussian smoothing was used in the Hybrid II algorithm, the shortest wavelength modes ($k \rho_i > 1$) affected by the filter (but not completely suppressed) were numerically unstable. We believe that this numerical instability is related to the instability observed when $\beta_e m_i / m_e < 1$ in all of the hybrid algorithms, which is associated with the backwards solution of Ampere's law in Eq.(14) that becomes ill-posed in the electrostatic limit. With adequate filtering, the ITG instability saturates in the simulations; and the thermal flux across the pressure gradient and the linear growth rates decrease together as a function of increasing β_e . The decrease in ion thermal flux accompanying the decrease in linear

growth rates as a function of increasing β_e was observed in earlier particle simulations using implicit methods and justified on the basis of a quasilinear argument in Ref. 9. Figure 8 shows the time histories of the fastest growing linear mode and the cross-field ion thermal flux. Figure 9 displays the accompanying mode energy spectrum at saturation showing the dominance of the radial mode and that an inverse cascade to longer wavelengths has occurred (although the truncated mode spectrum in these small “toy” simulations is severely limited). The ion thermal fluxes (not time-averaged or filtered) exhibit bursts of transport often seen in ITG simulations. In sum, the Hybrid II nonlinear simulations of the ITG instability with adequate filtering, particle statistics, and temporal resolution exhibit well-behaved saturations and credible physics results.

IV. TIME-STEP CONSIDERATIONS

To understand the additional computational burden due to the inclusion of kinetic electrons, we examine the time-step considerations associated with the three Courant conditions governing either accuracy or stability that arise from (1) the parallel electron motion $v_e \Delta t_e / \Delta x_{\parallel} = O(1)$, (2) the parallel ion motion $v_i \Delta t / \Delta x_{\parallel} = O(1)$, and (3) the parallel shear-Alfvén wave propagation $v_A \Delta t / \Delta x_{\parallel} < 1$. Taking into account that $\Delta x_{\parallel} = (B_0 / B_y^{(0)}) \Delta y = \theta^{-1} \Delta y$ in the two-dimensional slab, the Alfvén stability condition is $\theta v_A \Delta t / \Delta y < 1$. We note that

$v_e / v_A = (\beta_e m_i / m_e)^{1/2}$ and $v_i / v_A = (\beta_e T_i / T_e)^{1/2}$. With electron subcycling in the conventional δf simulation ($\Delta t / \Delta t_e = N_{sub}$), satisfying the Alfvén Courant condition implies reasonable

values for the electron parallel Courant condition, e.g., for $T_e = T_i$, $N_{sub} = 5$, $\theta = 0.01$, and

$\theta v_A \Delta t / \Delta y = 0.5$, then for $\beta_e = 0.1\%$ $v_e / v_A = 1.35$ $\theta v_e \Delta t_e / \Delta y = 0.135$; and

$\beta_e = 10\%$ $v_e / v_A = 13.5$ $\theta v_e \Delta t_e / \Delta y = 1.35$ With $v_e \Delta t_e / \Delta x_{\parallel} = O(1)$ our simulations are

well-behaved, and self-heating and numerical diffusion of the electron velocity distribution are acceptably small.¹⁷

Some recent papers introducing new particle-in-cell algorithms hope to relax the electron Courant condition to allow larger time steps.^{6,11} The introduction of split weights replaces the bulk thermal response of the electrons with a fluid response, and the non-adiabatic kinetic contribution to the perturbed distribution function is only significant for $v_{\parallel} - \omega / k_{\parallel} < v_e$ for the drift-wave phenomena of interest here. The hope is that the use of split weights will result in time step constraints only set by the relatively slow resonant electrons and that the weights of the fast thermal electrons will remain small and inconsequential. (Of course, the Alfvén Courant condition must still be satisfied; and the time step must be small enough so that electron self-heating and numerical orbit diffusion are insignificant.) However, using a larger time step for the thermal electrons (which are still represented with test particles) can result in those electrons inadequately sampling the peaks and valleys of the parallel electric field; and in consequence orbit diffusion will occur leading to stochastic heating of the thermal electrons and a growth of errors in their weights and contributions to the dielectric response.^{17,18} Just how restrictive is the electron Courant condition in our simulations? In Figure 10 we show results for Hybrid II simulations of the ITG and collisionless-drift instabilities in which the frequencies and growth rates of a single small-amplitude mode are plotted as a function of time step in the simulation. Hybrid II simulations of ITG retain some sensitivity to electron kinetics: $v_e \Delta t / \Delta y_{\parallel} = 1.5$ is needed for accurate simulations of a system with $\eta_i = \eta_e = 4$, $\beta_e = 0.035$, 32×32 grid, $m_i/m_e = 1837$, $k_y \rho_s = 1/8$, $\theta = 0.01$, $\rho_s/L_n = 0.1$, and no magnetic shear; and we note that there is no electron subcycling. The collisionless drift wave is more sensitive to electron kinetics: $v_e \Delta t / \Delta y_{\parallel} = 0.3$ is needed to accurately simulate a system with $\beta_e = 0.0049$, 16×16 grid, $m_i/m_e = 1837$, $k_y \rho_s = 1/4$, $\theta = 0.01$, $\rho_s/L_n = 0.2$, and no magnetic shear.

In practice the convergence of nonlinear simulations of drift-wave instability driven transport may set the most restrictive condition on time step, and the time step will depend on the parameters and physical conditions of the particular problem.¹⁹ We consider examples in Fig. 11 of nonlinear, many-mode, two-dimensional slab Hybrid II simulations as a function of time step. The simulation parameters were $\Delta t c_s / L_T = 0.4, 0.2, 0.1$; $\beta_e = 2.2 \times 10^{-3}$; no magnetic shear; $\theta = 0.01$; $T_e = T_i$; $\eta_i = \eta_e = 4$; $\rho_s / L_n = 0.1$; $\Omega_e / \omega_{pe} = 1$; $m_i / m_e = 1836$; $\rho_s = x$; 16×16 grid; and Heaviside-function mode filtering with $a=1$. For these parameters we can relate $\Delta t c_s / L_T$ to $v_e \Delta t / \Delta y_{||}$:

$$\Delta t c_s / L_T = (\Delta y / L_T) (m_e / m_i) \left(B_0 / B_y^{(0)} \right) v_e \Delta t / \Delta y_{||} \quad 0.2 v_e \Delta t / \Delta y_{||}.$$

If the time step is not chosen adequately small to resolve the nonlinear physics, one observes that in the supposedly saturated state there is a slow, secular, residual growth of the electrostatic and vector potential mode energies and a concomitant slow growth of the averaged cross-field thermal fluxes. We find it interesting that the accuracy constraints on the linear dispersion for ITG and collisionless drift-wave simulations in Fig. 10 set time step conditions $v_e \Delta t / \Delta y_{||} < 0.5$ that translate into $\Delta t c_s / L_T < 0.1$. These time steps are in keeping with the converged results for the nonlinear simulations in Fig. 11 and within the range of time steps typically used for the nonlinear toroidal gyrokinetic simulations in Ref. 19 which had gyrokinetic ions and adiabatic electrons. The experience presented here is encouraging for the addition of kinetic electrons and electromagnetic coupling to toroidal gyrokinetic simulations. However, we note that there are additional considerations that can influence the time step in toroidal simulations, which are not addressed here.

V. DISCUSSION

Achieving the goal of experimentally relevant simulations of turbulent transport in magnetically confined plasmas with a more complete physics model is very challenging. Including both electron and ion kinetic effects using a realistic mass ratio and accommodating a low-frequency electromagnetic model of the self-consistent electromagnetic fields in the plasma add significant complexity to the simulation models. The algorithms introduced here attempt to capture the physics of low-frequency ($\omega \ll \Omega_i$) drift-wave phenomena, the coupling to kinetic Alfvén waves that occurs at finite plasma pressure, and linear and nonlinear electron and ion kinetic phenomena (e.g., Landau resonance, particle trapping, induced Compton scattering).

For kinetic simulations to provide credible results there are a number of accuracy issues that restrict the time steps and grid resolution used:

$$k v_{E \times B} \Delta t < 1 \quad k \Delta x < 1 \quad k_{\parallel} \Delta x_{\parallel} < 1 \quad \omega \Delta t < 1 \quad \Delta x \leq \rho_{i,s} \quad k_{\parallel} v_s \Delta t < 1 \quad (20)$$

where $v_s = (T_s/m_s)^{1/2}$ is the thermal velocity for each species. The first condition in (20) is representative of a restriction on resolving finite-amplitude phenomena. We showed in Sec. IV that obtaining well-behaved nonlinear saturated states for the example of the ITG instability can set the most severe constraint that limits the time step in a given simulation. There is also the stability constraint set by $k_{\parallel} v_A \Delta t < 1$ for $v_A > c_s$. We have demonstrated that in the conventional δf simulation there is a constraint on resolving the skin depth c/ω_{pe} with the grid spacing in order to accurately reproduce the linear dispersion relation of shear-Alfvén waves and the drift instabilities. Because $\rho_i/(c/\omega_{pe}) = (T_i/T_e)^{1/2} (\beta m_i/m_e)^{1/2}$, the skin depth c/ω_{pe} becomes smaller than $\rho_i \sim \rho_s$ when $\beta_e m_i/m_e > 1$. Note that $c/\omega_{pe} = 0.05$ cm for $n_e = 10^{14}/\text{cm}^3$. Thus, resolving the skin depth becomes a more severe and onerous constraint than $\Delta x \leq \rho_s$ for

$\beta_e m_i / m_e > 1$. The hybrid algorithms introduced are not constrained to resolve the skin depth with the spatial grid, but these algorithms behave well only for $\beta_e m_i / m_e \gg 1$. With magnetic shear (not addressed here), populating the resonant electron layer with particles can become an additional important accuracy constraint on the simulations:⁹

$\Delta x_e \sim (k_{\parallel} / k_y) L_s \sim (\omega / k_y v_e) L_s \sim (m_e / m_i)^{1/2} (L_s / L_n) \rho_s$. When there is a discrete resonance layer, then a Landau fluid or continuum Vlasov code must resolve this layer with its spatial grid to capture the electron Landau resonance.

The results presented here indicate that significant progress is being made in adding kinetic electron and electromagnetic effects to multi-dimensional gyrokinetic ion simulations of core turbulent transport. Simulations with δf gyrokinetic ions and drift-kinetic electrons using parallel canonical momentum including coupling of the drift-waves and sound waves to the kinetic shear-Alfvén waves yielded results in good agreement with linear theory for (1) kinetic shear-Alfvén waves, (2) the collisionless drift wave instability, and (3) the ion temperature drift instability (including finite- β stabilization effects on the latter two drift-wave instabilities) if the cell size was smaller than the skin depth in the unsheared slab cases studied. These results agree with those obtained in Refs. 8 and 9.

The Hybrid II algorithm yielded good results for finite β_e , $\beta_e m_i / m_e > 1$, and did *not* require that the cell size be smaller than the skin depth c/ω_{pe} , but led to a numerical instability for $\beta_e m_i / m_e < 1$. Hybrid II was the best of the hybrid algorithms investigated here on the basis of its good performance in the test cases. Both the conventional δf and kinetic-extended hybrid algorithms have restrictions on the time step used to recover the correct dielectric responses and to produce converged nonlinear steady states. However, similar non-dimensional time steps are required in three-dimensional nonlinear toroidal gyrokinetic simulations with adiabatic electrons.

Thus, nonlinear electromagnetic simulations of drift-wave turbulence and transport with kinetic electrons using the Hybrid II algorithm introduced here appear to be tractable.

Acknowledgments

This work was supported by the U.S. Department of Energy under Contract No. W-7405-ENG-48 at the University of California Lawrence Livermore National Laboratory. We thank J.-N. Leboeuf, L. Chen, G. Hammett, P. Snyder, W. Lee, and Z. Lin for useful discussions. This research is a part of the Plasma Microturbulence Project sponsored by the DOE Office of Fusion Energy Sciences.

APPENDIX A: HYBRID I AND III ALGORITHMS

A. Hybrid I Algorithm

In Chen and Parker’s hybrid algorithm² gyrokinetic ions and a “massless” electron fluid model following earlier work in Ref. 16 were combined to allow electromagnetic simulation of the ion temperature gradient instability with electromagnetic coupling to the shear-Alfvén wave and finite- β stabilization. Here we extend the Chen and Parker algorithm to include drift-kinetic electrons.

Consider the modified electron momentum equation (Ohm’s law) in Eq.(13a) with

$$\parallel P_{\parallel e} = \parallel \left(P_{\parallel e}^{(0)} + \delta P_{\parallel e}^K \right) + T_{\parallel e}^{(0)} \parallel \left(\delta n_e - \delta n_e^K \right), \quad (\text{A1})$$

where $T_{\parallel e}^{(0)}$ is a constant, δn_e^K and $\delta P_{\parallel e}^K$ are the total density and parallel pressure moments of the δf perturbed electron distribution function, and δn_e is the total perturbed electron density. The additional term in the parallel gradient of the pressure, $T_{\parallel e}^{(0)} \parallel \left(\delta n_e - \delta n_e^K \right)$, is zero in the limit that the total perturbed electron density is converged to that accumulated directly from the

particle electrons. This is a computational artifice very similar to semi-implicit modifications sometimes introduced to improve convergence or stability. Equations (13a) and (A1) can be rewritten to provide some insight into the model adopted for the parallel pressure and the kinetic electron corrections:

$$T_{\parallel e}^{(0)} \delta n_e = T_{\parallel e}^{(0)} \delta n_e^K + \left(\parallel (P_{\parallel e}^{(0)} + \delta P_{\parallel e}^K) + en_{0e} \vec{\mathbf{E}} \cdot \hat{\mathbf{b}} + n_{0e} m_e (\partial / \partial t + \vec{v} \cdot \nabla \times \mathbf{B}) u_{\parallel} \right), \quad (\text{A2})$$

where the first term on the right is dominant over the remainder of the right side which is small. Thus, the modified momentum equation Eq.(13a) is constructed to ensure that the parallel gradient of the total perturbed electron density is a good approximation to the parallel gradient of the fully kinetic perturbed electron density. The Chen and Parker hybrid scheme used a fluid representation of the parallel gradient of the pressure given by

$$\parallel P_{\parallel e} = \parallel P_{\parallel e}^{(0)} + T_{\parallel e}^{(0)} \delta n_e + n_{0e} \parallel \delta T_e \text{ with the constraint introduced in Ref. 16:}$$

$$\parallel (T_{\parallel e}^{(eq)} + \delta T_{\parallel e}) = 0, \text{ where } T_{\parallel e}^{(eq)} \text{ is the equilibrium parallel electron temperature including any}$$

gradients and $P_{\parallel}^{(0)} = n_e^{(0)} T_e^{(eq)}$. With the use of this constraint, there is no difference

between $\eta_e = 0$ and $\eta_e \neq 0$ in Chen and Parker's algorithm; and Chen and Parker only considered systems with $\eta_e = 0$. The Hybrid I kinetic extension of the Chen and Parker algorithm introduced here is likewise constrained to $\eta_e = 0$ and is numerically unstable for finite η_e .

We next solve Eq.(13) for $\partial A_z / \partial t = c(\vec{\mathbf{E}} + \nabla \phi) \cdot \hat{\mathbf{b}}^{(0)} = \dots$, which is used to advance A_z in time. Ampere's law Eq.(14) and electron continuity Eq.(15) determine $u_{\parallel e}$ and δn_e , respectively. The electrostatic potential is determined by the solution of Eq.(8) in the quasi-neutral limit. The gyrokinetic ions and the drift-kinetic electrons are advanced with the parallel velocity

representation and no electron subcycling using Eq.(16a) for the ions and the following equation for the electrons obtained from the drift-kinetic equation for electrons with split weights:

$$\frac{dw_j^e}{dt} = \frac{-ev_{\parallel}}{T_e} \vec{\mathbf{E}} \cdot \hat{\mathbf{b}} - \kappa_e \left(\frac{c}{B} \frac{\partial \phi}{\partial y} - \frac{v_{\parallel} \tilde{B}_x}{B} \right), \quad (\text{A3})$$

B. Hybrid III Algorithm

Here we introduce a third kinetic electron extension of the Chen and Parker hybrid algorithm. In this algorithm we again employ the split-weight electron distribution function Eq.(1)⁶ and consider the electron fluid momentum equation Eq.(13a). However, we introduce a revised definition of the gradient of the parallel pressure:

$$\parallel P_{\parallel e} = \parallel P_{\parallel e}^{(0)} + T_{\parallel e}^{(0)} \parallel \delta n_e + \parallel \Delta P_{\parallel e}^K, \quad (\text{A4})$$

where $T_{\parallel e}^{(0)}$ is a constant, $\Delta P_{\parallel e}^K = d^3 \mathbf{v} h_e v_{\parallel}^2$ is the non-adiabatic kinetic electron parallel pressure *increment* for the electrons, and δn_e is the total perturbed electron density. We note that the parallel pressure used in Eq.(A4) is consistent with the pressure moment of the split-weight electron distribution function. As in the other two hybrid algorithms, Equations (13a) and (A4) along with $\partial A_z / \partial t = c(\vec{\mathbf{E}} + \phi) \cdot \hat{\mathbf{b}}^{(0)}$ are used to advance A_z in time. Ampere's law Eq.(14) and electron continuity Eq.(15) again determine $u_{\parallel e}$ and δn_e . The electrostatic potential is determined by the solution of Eq.(8) in the quasi-neutral limit. The gyrokinetic ions and the drift-kinetic electrons are advanced with the parallel velocity representation and no electron subcycling using Eq.(16a) for the ions and the following equation for the electrons obtained from the drift-kinetic equation for electrons with split weights (after cancellations obtained by using both the fluid momentum and the continuity equations)

$$\begin{aligned} \frac{dw_j^e}{dt} = & (\bar{\kappa}_e - \bar{\kappa}_{ne}) \bar{\mathbf{v}}_{\mathbf{E} \times \mathbf{B}} + (\kappa_e - \kappa_{ne} - \kappa_{Te}) v_{\parallel} \frac{\delta B_x}{B_0} + \parallel u_{\parallel e} \\ & + (v_{\parallel} / n_{0e} v_e^2) \parallel \Delta P_{\parallel e}^K + (v_{\parallel} / v_e^2) (\frac{\partial}{\partial t} + \bar{\mathbf{v}}_{\mathbf{E} \times \mathbf{B}} \cdot \nabla) u_{\parallel e}. \quad (\text{A5}) \end{aligned}$$

Because this algorithm, which is similar to the Hybrid II scheme, uses the split-weight representation, particle noise in the electrons enters only through the non-adiabatic response h_e in the distribution function. However, in contrast to the Hybrid II algorithm, Hybrid III requires the second parallel velocity moment of h_e , which is intrinsically noisier than the number density moment used in Eq.(13b). The $\Delta P_{\parallel e}^K$ moment tends to be more problematic for the drift-wave phenomena of interest at finite plasma pressure because of the small parallel phase velocities (only for these velocities is h_e expected to be appreciable) compared to the electron thermal velocity. Furthermore, like the Hybrid I algorithm, the Hybrid III algorithm was numerically unstable for finite η_e .

C. Discussion of the Hybrid Algorithms

The Hybrid I and II algorithms were introduced which add kinetic electron closures to the Chen-Parker hybrid electromagnetic scheme.² These algorithms yielded good results in all three test cases for finite β_e , $\beta_e m_i / m_e > 1$, and did *not* require that the cell size be smaller than the skin depth c/ω_{pe} , but led to a numerical instability for $\beta_e m_i / m_e < 1$. Data produced by all three hybrid schemes is posted at <http://www.mfescience.org/mfedocs/> in a document UCRL-JC-142446. The Hybrid III algorithm using a kinetic pressure closure adequately simulated the kinetic shear-Alfvén wave and the ion-temperature-gradient instability (constrained to $\eta_e = 0$), but so far has failed to yield acceptable results for the collisionless drift wave.

Solving for the electron density in the electron momentum fluid equation provides insight into the behavior of the three hybrid algorithms,

$$\text{Hybrid I: } T_{\parallel e}^{(0)} \delta n_e = -en_{0e} E_{\parallel} - \parallel (P_{\parallel e}^{(0)} + \delta P_{\parallel e}^K) - inertia + T_{\parallel e}^{(0)} \parallel \delta n_e^K,$$

$$\text{Hybrid II: } T_{\parallel e}^{(0)} \delta n_e = (-en_{0e} E_{\parallel} - \parallel P_{\parallel e}^{(0)} - n_{0e} \parallel \delta T_{\parallel e}) - inertia + T_{\parallel e}^{(0)} \parallel \Delta n_e^K,$$

$$\text{Hybrid III: } T_{\parallel e}^{(0)} \delta n_e = -en_{0e} E_{\parallel} - \parallel (P_{\parallel e}^{(0)} + \Delta P_{\parallel e}^K) - inertia.$$

The Hybrid I and II algorithms have better leverage because they use δn_e^K and Δn_e^K which are much better resolved statistically than is $\Delta P_{\parallel e}^K / v_e^2$ in Hybrid III. The resulting response for δn_e in Hybrid I is the sum of fluid terms (that nearly cancel if the fluid momentum equation is a reasonable approximation to the ensemble of particle electron trajectories) plus the term coming from the kinetic electron density collected from the particles. In the Hybrid II algorithm δn_e is equal to the sum of the fluid terms constituting the appropriate adiabatic response plus the inertial and kinetic incremental corrections. In the Hybrid III algorithm δn_e equals the correct adiabatic response plus both a small increment from the inertia terms and a kinetic increment coming from $\Delta P_{\parallel e}^K$ which is more prone to error than using a kinetic charge density moment (a lower moment of h_e). We believe that the difficulties in the Hybrid I and III algorithms with finite η_e derive from a computational incompatibility between the dual fluid and particle representations of the electrons and from relative errors in computing the pressure moment of the electron distribution. The Hybrid I and III algorithms are constrained by the assumption that finite- η_e effects are negligible and require $\eta_e = 0$, while Hybrid II accommodates $\eta_e \neq 0$.

References

- ¹W. W. Lee, J. Comput. Phys. **72**, 243 (1987).
- ²Y. Chen and S. Parker, Phys. Plasmas **8**, 441 (2001).
- ³M. Kotschenreuther, Bull. Am. Phys. Soc. **34**, 2107 (1988); R. E. Denton and M. Kotschenreuther, J. Comput. Phys. **119**, 283 (1995).
- ⁴A. M. Dimits and W. W. Lee, J. Comput. Phys. **107**, 309 (1993).
- ⁵B. I. Cohen, T. J. Williams, A. M. Dimits, and J. A. Byers, Phys. Fluids B **5**, 2967 (1993).
- ⁶I. Manuisky and W. W. Lee, Phys. Plasmas **7**, 1381 (2000).
- ⁷J. V. W. Reynders, Ph.D. thesis, Princeton University (1992).
- ⁸J. C. Cummings, Ph.D. thesis, Princeton University (1995).
- ⁹B. I. Cohen and A. M. Dimits, Phys. Rev. E **56**, 2151 (1997).
- ¹⁰Y. Chen and S. E. Parker, Phys. Plasmas **8**, 2095 (2001).
- ¹¹Z. Lin and L. Chen, Phys. Plasmas **8**, 1447(2001).
- ¹²T. S. Hahm, W. W. Lee, and A. Brizard, Phys. Fluids **31**, 1940 (1988).
- ¹³E. A. Frieman and L. Chen, Phys. Fluids **25**, 502 (1982).
- ¹⁴W. W. Lee, Phys. Fluids **26**, 556 (1983).
- ¹⁵B. I. Cohen, T. A. Brengle, D. B. Conley, and R. P. Freis, J. Comp. Phys. **38**, 45 (1980); B. J. U. Brackbill and B. I. Cohen, *Multiple Time Scales*, Computational Techniques (Academic Press Inc., Orlando, 1985), Chapt. 10.
- ¹⁶S. E. Parker, J. C. Cummings, W. W. Lee and H. E. Mynick, in *Joint Varenna-Lausanne 15th International Workshop on Theory of Fusion Plasmas*, August 22-26, 1994 (Editrice Compositori for Italiana di Fisica, Bologna, 1994)]; P. B. Snyder, Ph.D. thesis, Princeton U., 1999; P. B. Snyder and G. W. Hammett, Phys. Plasmas **8**, 744 (2001).
- ¹⁷C. K. Birdsall and A. B. Langdon, *Plasma Physics Via Computer Simulation* (McGraw-Hill,

New York, 1985), Ch. 8.

¹⁸A. B. Langdon, J. Comput. Phys. **30**, 202 (1979).

¹⁹A. M. Dimits, G. Bateman, M. A. Beer, B. I. Cohen, W. Dorland, G. W. Hammett, C. Kim, J. E. Kinsey, M. Kotschenreuther, A. H. Kritz, L. L. Lao, J. Mandrekas, W. M. Nevins, S. E. Parker, A. J. Redd, D. E. Shumaker, R. Sydora, and J. Weiland, Phys. Plasmas **7**, 969 (2000).

TABLE I. ITG frequencies and growth rates normalized to the ion cyclotron frequency for $\eta_e=0$ and $\eta_e=4$, $\eta_i=4$, $\Omega_e/\omega_{pe}=1$, $m_i/m_e=1836$, $\rho_s/L_n=0.1$, $B_y^{(0)}/B_0=0.01$, $T_e=T_i$, and $\beta_e=0.0547\%$ and 3.54% .

β_e	η_e	theory ($Re\omega/\Omega_i$, $Im\omega/\Omega_i$)	Hybrid II simulation ($Re\omega/\Omega_i$, $Im\omega/\Omega_i$)
0.0547%	0	(-0.00412, 0.00640)	(-0.0039, 0.0061)
0.0547%	4	(-0.00304, 0.00601)	(-0.0030, 0.0059)
3.54%	0	(-0.00313, 0.00285)	(-0.0033, 0.0029)
3.54%	4	(-0.00287, 0.00265)	(-0.0029, 0.0028)

Figure Captions

Figure 1. Frequencies and damping rates from conventional δf simulations of kinetic shear-Alfvén waves as functions of the ratio of the cell size to the skin depth and the electron β_e .

Figure 2. Frequencies and damping rates from Hybrid II and III simulations of kinetic shear-Alfvén waves as functions of the electron β_e .

Figure 3. Frequencies and growth rates from conventional δf simulations of the collisionless drift-wave instability as functions of the electron β_e with the grid cell size smaller than the skin depth.

Figure 4. Frequencies and growth rates from conventional δf simulations of the collisionless drift-wave instability as functions of the ratio of the cell size to the skin depth and the electron β_e .

Figure 5. Frequencies and growth rates from Hybrid II () and conventional δf (O) simulations of the collisionless drift-wave instability as functions of the ratio of the cell size to the skin depth and the electron β_e .

Figure 6. Frequencies and growth rates from conventional δf simulations of the ion-temperature-gradient instability as functions of the ratio of the cell size to the skin depth and the electron β_e .

Figure 7. Frequencies and growth rates from Hybrid II simulations (with $\eta_e=4$) of the ion-temperature-gradient instability as functions of the electron β_e .

Figure 8. The spatially averaged ion thermal fluxes in x normalized to the sound speed and the modulus of the Fourier amplitude of the electric potential for the fastest growing mode from conventional δf and Hybrid II nonlinear simulations of the ion-temperature-gradient instability as functions of time for three simulations at different values of β_e .

Figure 9. The modulus of the Fourier amplitude of the electric potential as a function of k_y for $k_x=1$ (both normalized to $\Delta k = \pi/8$) averaged in time after saturation in three δf and Hybrid II nonlinear simulations of the ion-temperature-gradient instability for different values of β_e .

Figure 10. Frequencies and growth rates from Hybrid II simulations of the ion-temperature-gradient and collisionless drift-wave instabilities as functions of the relative time step.

Figure 11. The spatially averaged ion thermal fluxes in x normalized to the sound speed and the modulus of the Fourier amplitude of the electric potential for the fastest growing mode from conventional Hybrid II nonlinear simulations of the ion-temperature-gradient instability as functions of time for three simulations at different values of the relative time step. The observed linear growth rates are indicated.

Figure 1

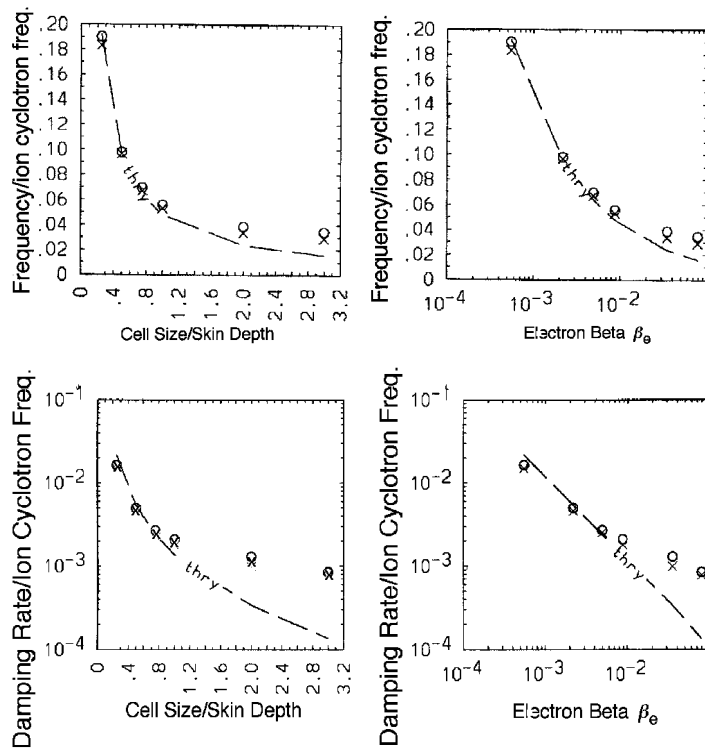


Figure 2

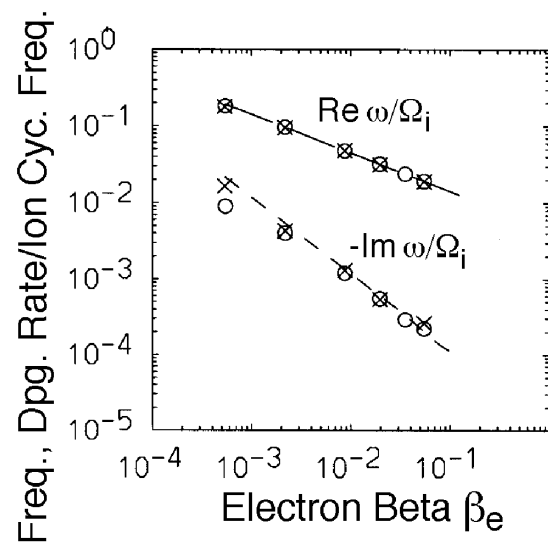


Figure 3

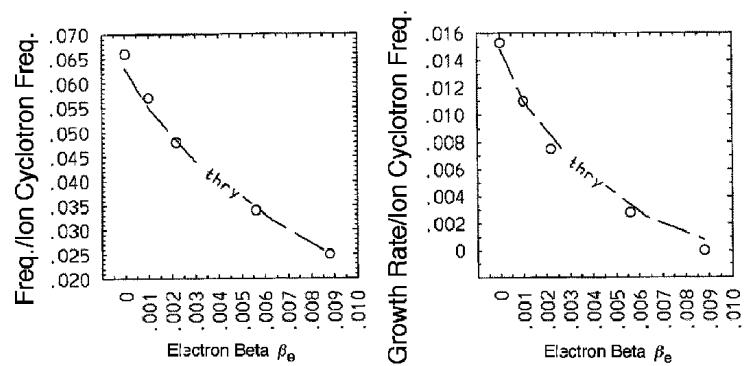


Figure 4

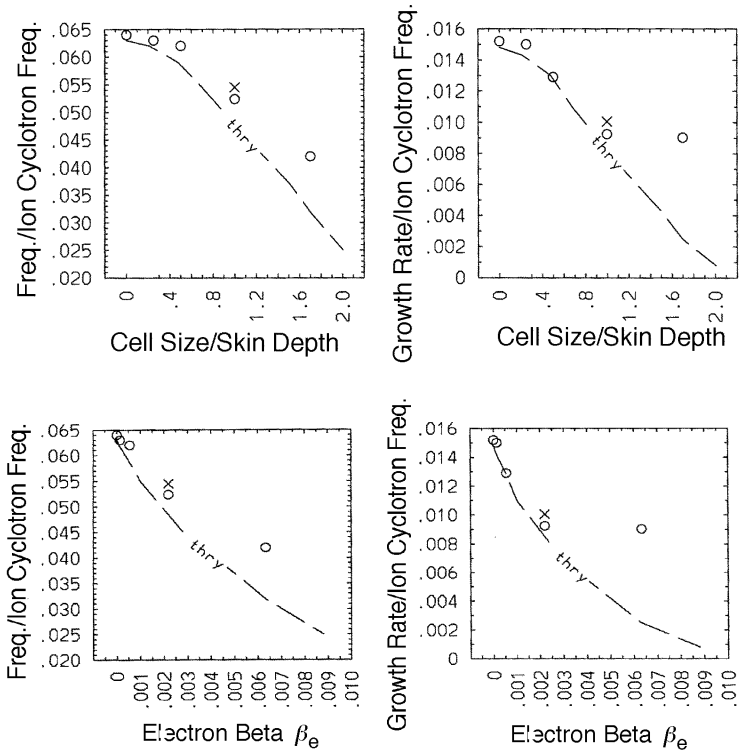


Figure 5

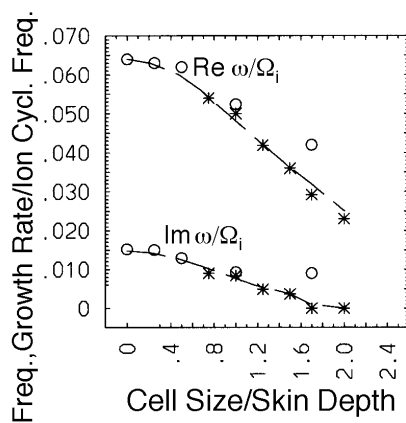
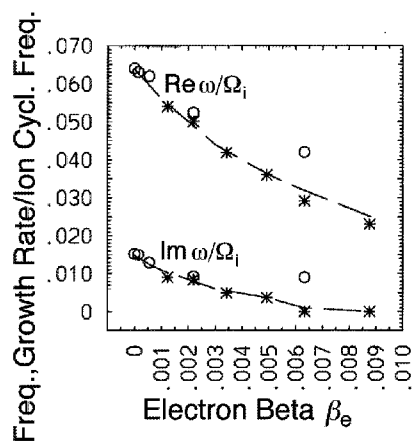


Figure 6

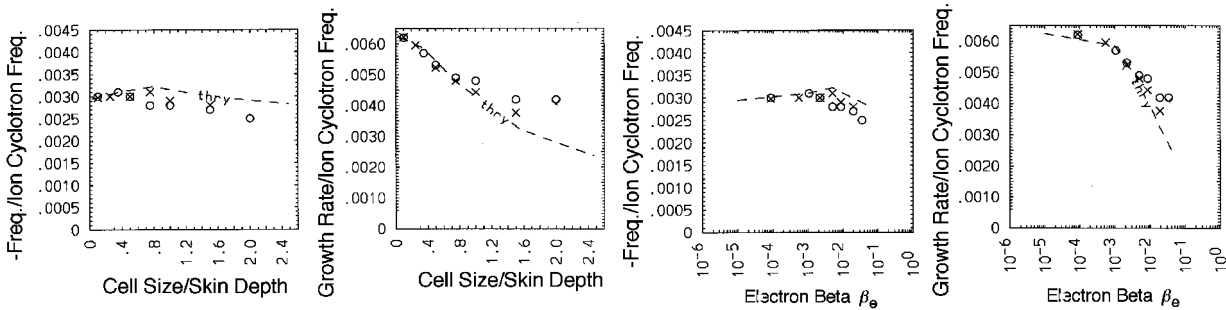


Figure 7

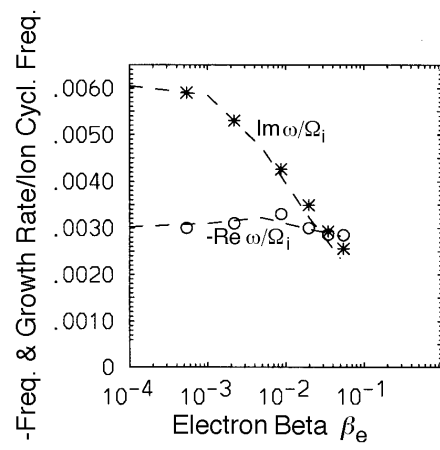


Figure 8

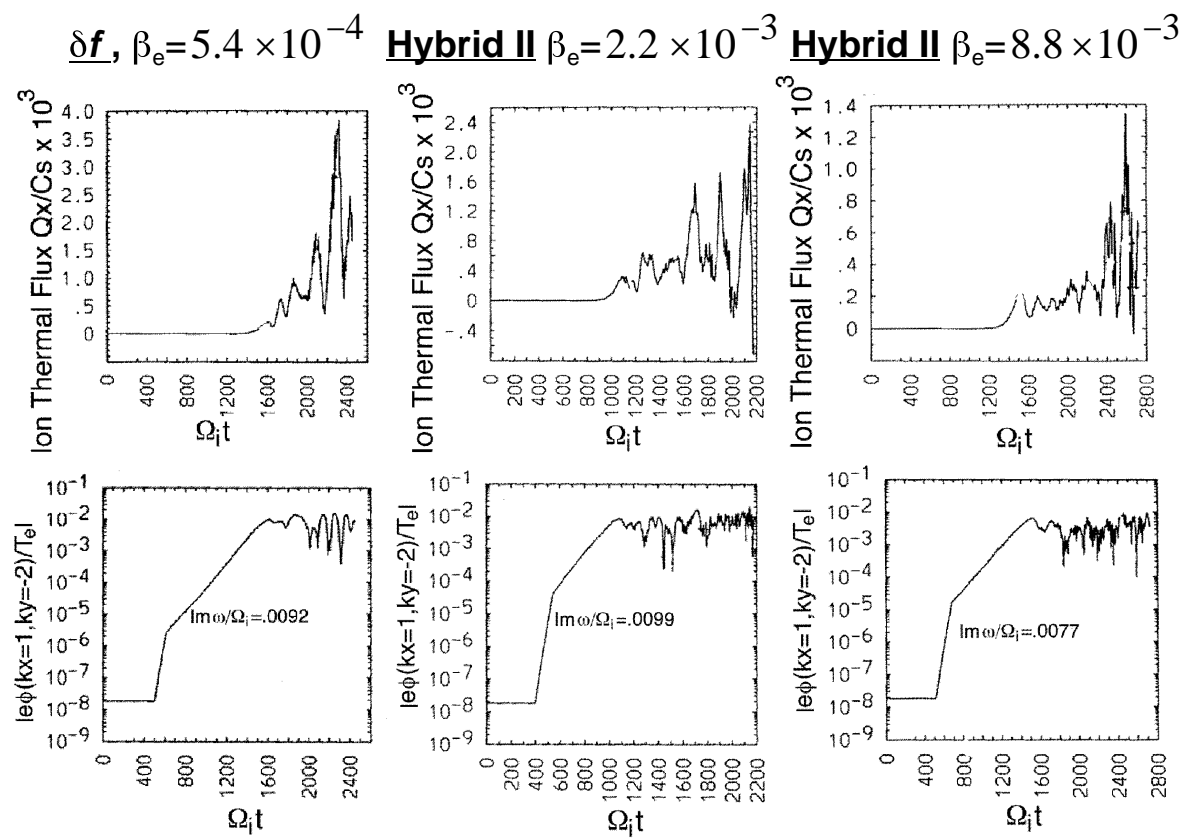


Figure 9

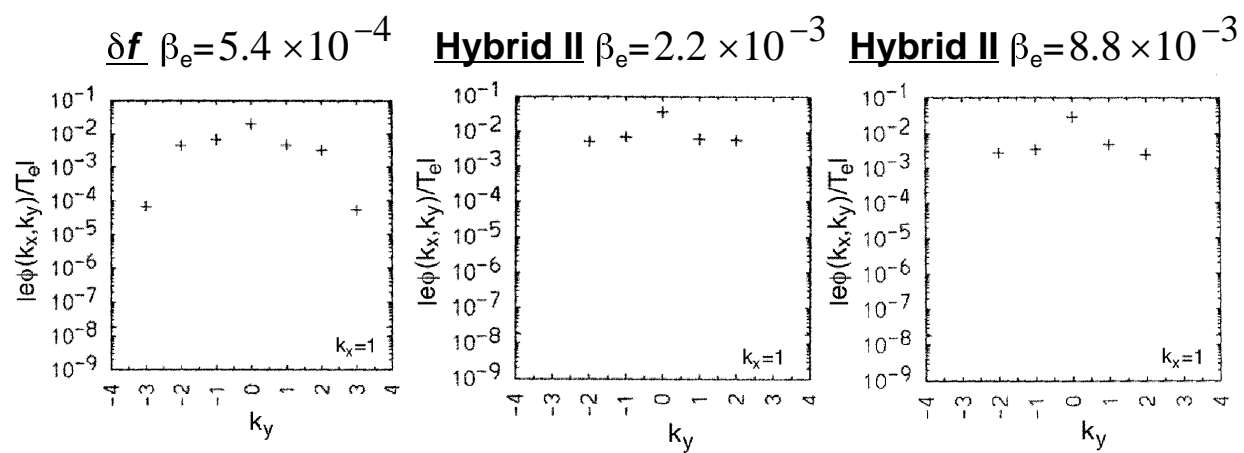


Figure 10

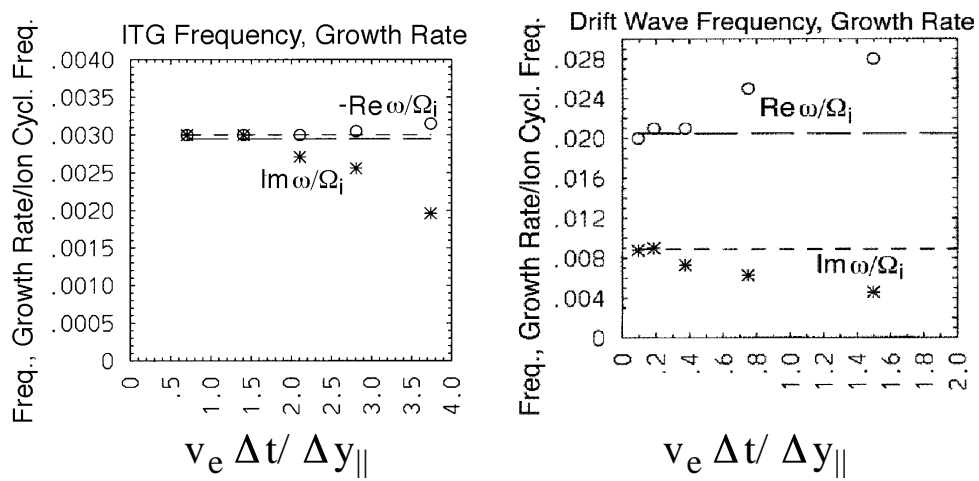


Figure 11

